Tumor visualization and evaluation of glioblastoma in mice using small animal 9.4T MRI and PET-CT with high resolution

SHUANGYI LI[1*], WENJIAO GU[1*], YING JIANG[1], TING LIU[2,3], LIMEI SHUAI[2,3], YUJIE WEI[2], YOUMING SHI[1], HAVYARIMANA JUVENAL[1], ZHIMIN WANG[4], YUCAI WEI[2], BOFAN WU[5], XIAOCHUN ZHOU[1,6], YUMIN LI[2] and FUTIAN TANG[1,2]

[1]Department of Cardiovascular Disease, The Second Hospital & Clinical Medical School, Lanzhou University, Lanzhou, Gansu 730030, P.R. China; [2]Gansu Province Key Laboratory of Environmental Oncology, The Second Hospital & Clinical Medical School, Lanzhou University, Lanzhou, Gansu 730030, P.R. China; [3]Gansu Provincial Key Laboratory of Environmental Oncology, School of Basic Medical Sciences, Lanzhou University, Lanzhou, Gansu 730030, P.R. China; [4]Department of PET/CT Center, Gansu Provincial People's Hospital, Lanzhou, Gansu 730030, P.R. China; [5]Wuhan United Imaging Life Science Instrument Co., Ltd., Wuhan, Hubei 430206, P.R. China; [6]Department of Nephrology, The Second Hospital & Clinical Medical School, Lanzhou University, Lanzhou, Gansu 730030, P.R. China

Received May 21, 2025; Accepted December 23, 2025

DOI: 10.3892/or.2026.9076

Abstract. Glioblastoma (GBM) is the most prevalent type of malignant primary brain tumor. Preclinical research serves a key role in investigating the development and mechanism of GBM tumor. However, the dynamic and non-invasive evaluation of tumors in animals faces challenges, such as the limited sensitivity of clinical instruments and insufficient spatial resolution for mouse brain tumors. The present study aimed to establish an *in vivo* mouse GBM model and evaluate the model using high resolution small animal positron emission tomography-computed tomography (PET-CT) and magnetic resonance imaging (MRI). Metabolism was compared between the normal brain and tumor tissue by using ^{1}H-magnetic resonance spectroscopy (^{1}H-MRS). T2-weighted imaging (T2WI) MRI detected the tumor in the brain 7 days after injection of GL261 cells, with tumor sizes of 1.263, 4.917 and 13.85 mm^3 on days 7, 14 and 21, respectively. ^{1}H-MRS demonstrated that the levels of tissue metabolites such as lactate and total choline increased, while those representing neurological function of the brain such as total N-acetylaspartate decreased in tumor compared with the normal brain tissues. PET-CT imaging confirmed the tumor detected by MRI. At 6-120 min post ^{18}F-fluorodeoxyglucose (FDG) administration, the standard uptake value (SUV) in tumor tissue gradually increased, while the SUV value in normal brain tissue gradually decreased. SUV in the liver and kidneys decreased, while SUV in the bladder increased in a time-dependent manner. Pharmacokinetic analysis showed that the distribution of FDG in brain and tumor tissue conformed to a two-tissue compartment model. This model consists of a plasma compartment and two tissue compartments representing free FDG and phosphorylated FDG within brain or tumor tissue. The model parameters are defined as follows: Fractional blood volume (vB)=3.6%, k1 (forward transport rate)=1.844, k2 (reverse transport rate)=3.844 and k3 (phosphorylation rate)=0.280 in brain and vB=2.3%, k1=0.797, k2=2.722 and k3=0.319 in tumor tissue, respectively. The tumors observed by MRI and PET-CT imaging were ultimately confirmed through morphological and pathological analysis. Compared with normal brain tissue, glioma tissue exhibited significantly elevated glucose transporter type 1 protein levels. In conclusion, the model was confirmed by high-resolution small animal PET-CT and MRI, as well as morphological and pathological approaches.

Correspondence to: Professor Futian Tang, Department of Cardiovascular Disease, The Second Hospital & Clinical Medical School, Lanzhou University, 82 Cuiyingmen, Chengguan, Lanzhou, Gansu 730030, P.R. China
E-mail: tangft@163.com

Professor Yumin Li, Gansu Province Key Laboratory of Environmental Oncology, The Second Hospital & Clinical Medical School, Lanzhou University, 82 Cuiyingmen, Chengguan, Lanzhou, Gansu 730030, P.R. China
E-mail: liym@lzu.edu.cn

*Contributed equally

Key words: glioblastoma, mouse tumor model, PET-CT, MRI, ^{1}H-magnetic resonance spectroscopy

Introduction

Glioblastoma (GBM) is the most common primary malignancy of the central nervous system and is associated with poor prognosis (1-3). GBM accounts for 49% of all malignant primary brain and central nervous system tumors in adult patients (4), with ~13,000 cases diagnosed in the US each year (5). The disease has 5-year relative survival rate of 5% (6,7). Currently, early diagnosis and classification, precise intervention and easy prognosis assessment

of GBM are challenging due to difficulties in accurately delineating tumor boundaries, distinguishing tumor recurrence from treatment-related changes, and capturing intratumoral heterogeneity using conventional diagnostic approaches (6,8). Development and popularization of non-invasive imaging techniques such as magnetic resonance imaging (MRI) and positron emission tomography-computed tomography (PET-CT) serve an important role in the early diagnosis and prognostic assessment of GBM, potentially decreasing the morbidity and mortality of GBM (1,9). MRI can accurately locate the position of the tumor and characterize its metabolic profile by quantifying key metabolites, including choline-containing compounds, N-acetylaspartate, creatine, lactate and lipids, using MR spectroscopy (MRS) (10,11). Using PET-CT, the location of tumor can be shown after injecting specific nuclide tracers such as ^{18}F-fluorodeoxyglucose (FDG) (12,13). Simultaneously, the pharmacokinetics of FDG in both tumor and other tissue or organs can be analyzed and quantified by PET-CT imaging (14). However, research on the origin, progression, and pathology of GBM cannot be conducted in clinical setting because of ethical issues. Instead, preclinical study of tumor animal models is used to investigate the origin, growth and metastasis of GBM. With the advancement of high field small animal MRI and submillimeter-level high-resolution small animal PET-CT technology (14,15), new approaches and methodologies have emerged for preclinical research on brain glioma.

There are two commonly used tumor models of GBM in mice, including subcutaneous and *in situ* tumor model in the brain (16,17). Subcutaneous tumor is a simple model for preclinical evaluation of drug efficacy *in vivo* and also plays a key role in the study of tumor pathogenesis and drug action. This model is easy to operate and demonstrates the tumor growth process. However, the main limitation of this model is that the tumor is implanted and grows subcutaneously, having no associated tumor microenvironment. This limitation can be resolved by using the *in situ* tumor model, in which the GBM cells are directly injected into the brain. This model better simulates the microenvironment of tumor cells *in vivo* and simulates the process of tumor growth and metastasis. However, the tumor in the brain of mice cannot be easily detected without imaging technology such as MRI and PET-CT unless the mice are sacrificed (18,19). Humans have an average body weight of 60 kg, whereas mice have an average body weight of 25 g. Therefore, high field MRI and high-resolution PET-CT equipment specifically designed for small animals have emerged (13,20,21). These technologies have the advantages of detecting and monitoring the tumor in a visual, dynamic, non-invasive and quantitative manner, recording the tumor growth process to the maximum extent.

9.4 Tesla MRI (9.4T MRI) leverages an ultra-high magnetic field to acquire images with high spatial resolution and signal-to-noise ratio, making it a meaningful tool in preclinical biomedical research fields such as neuroscience and oncology. In an *in situ* GBM rat model using U87 cells, Yun *et al* (22) dynamically evaluated the antiangiogenic effect of bevacizumab using a 9.4T MRI scanner and found that the tumor volume in the brain of rats shown by T2-weighted imaging (T2WI) continuously increased in the time-dependent manner. In the same model, Nickel *et al* (23) scanned the brain on a 9.4T MRI and concluded that standard contrast agent dosage is sufficient to visualize the core tumor volume in T1WI MRI. Simultaneously, brain tumor metabolism was assessed non-invasively using ^{1}H-MRS.

FDG is valuable in the diagnosis and prognosis of GBM (24). In high-grade tumors, FDG uptake is typically elevated and several parameters can be evaluated, among which the maximum standardized uptake value (SUVmax) is the most commonly used in clinical diagnosis (10,25). SUVmax is associated with tumor prognosis as increased glucose consumption in tumors is associated with tumor grade, biological aggressiveness and patient survival in glioma (23). However, lesions in or adjacent to grey matter may be masked by high uptake in normal grey matter and there is an overlap in FDG uptake between low- and high-grade gliomas, so it is currently not possible to differentiate between tumor boundary and glioma grade or predict prognosis based on FDG PET alone (24). Combining FDG PET/CT with MRI improves the accuracy of tumor grading.

The integration of MR sequences with FDG PET/CT enables the evaluation of the association between parameters such as regional cerebral blood volume, choline-to-creatine ratio (Cho/Cr), N-acetylaspartate-to-choline ratio (NAA/Cho) and FDG SUVmax, and tumor genetics and histopathology. This comprehensive approach facilitates the determination of tumor malignancy by linking imaging-derived parameters (Cho/Cr, NAA/Cho and FDG SUVmax) to underlying biological processes, including cell proliferation, neuronal loss, altered energy metabolism, and tumor aggressiveness (23).

The present study aimed to establish an *in vivo* GBM mouse model and evaluate it using high resolution small animal PET-CT and 9.4T MRI, complemented by morphological and pathological validation. Metabolic alterations were further analyzed using ^{1}H-MRS.

Materials and methods

Animals and GBM model. The entire experimental process is shown in Fig. 1. The Ethics Committee on Animal Study of Lanzhou University Second Hospital (Lanzhou, China) approved the protocol (approval no. D2025-787). C57 mice (weight, 17-18 g) were purchased from Experimental Animal Center of Lanzhou University. Mice were housed in the specific-pathogen-free animal care facility of Lanzhou University Second Hospital under a 12/12-h light/dark cycle (lights on at 7:00 AM), an ambient temperature of 22±2˚C and a relative humidity of 50±10%. All mice were fed a standard diet and had *ad libitum* access to autoclaved drinking water. The animals were housed (3-5 mice/cage) in standard ventilated cages with corn cob bedding. A total of 18 male C57BL/6 mice (age, 8 weeks) were included (12 for MRI, with 6 assigned to the tumor group and 6 to the normal group; 6 for PET-CT, with 3 assigned to the tumor group and 3 to the normal group).

In the surgery, mice were anesthetized for 5 min using 3% isoflurane (2 l/min). Subsequently, anesthesia was maintained at 1-1.5% isoflurane (1 l/min) until the procedure was completed. The mice were placed on a thermal pad, and their heads were secured in a stereotaxic instrument. After the head

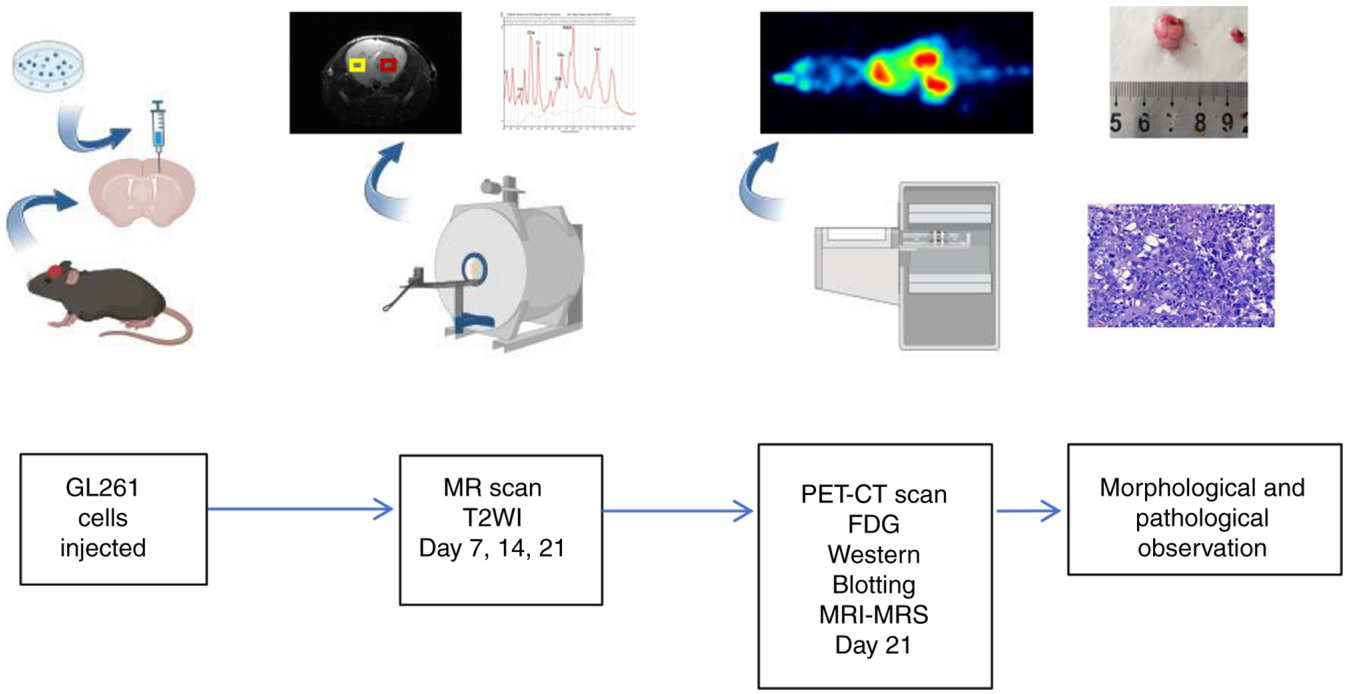

Figure 1. Experimental design. A total of 6 mice were orthotopically implanted with GL261 cells. A total of 7 days later, the tumor volume was determined using T2WI (red, tumor ROI; yellow, normal tissue ROI). Spectra were acquired with a short echo time point-resolved spectroscopy sequence. Small animal PET-CT was used to evaluate the model by injecting FDG via tail vein and analyze the pharmacokinetics of FDG. Western blot assay was performed for molecular-level analysis of GLUT1 protein expression. Morphological and pathological analyses were used to confirm the final result. FDG, ^{18}F-fluorodeoxyglucose; T2WI, T2-weighted imaging; ROI, region of interest; GLUT1, glucose transporter type1; ^{1}H-MRS, ^{1}H-magnetic resonance spectroscopy.

was sterilized with iodophor, the skin was cut longitudinally in accordance with the sagittal midline position; the length of the incision was ~1 cm, and the position corresponding to the right caudate nucleus was determined according to the anatomical map of the stereotaxic instrument: 2.0 mm anterior to the fontanel, 1.0 mm right to the midline and 3.5 mm subdural in depth. A hole was drilled with a skull drill without damaging the dura mater. A total of 5 μl (5x10^4 GL261 cells) cell suspension was injected using a glass electrode at an injection rate of 50 nl/sec. After the cell suspension was injected, the needle was retained for 10 min. The incision was sutured with a 5-gauge thread and sterilized with iodophor to prevent infection. Following surgery, mice were kept on a heating pad until full recovery from anesthesia and monitored closely for the first 6 h. Health and behavioral assessments were conducted every 2 days initially, with the frequency increasing to daily from day 14 onward. Humane endpoints requiring immediate euthanasia included weight loss >20% of peak body weight. No mice died during the 21 day experimental period following the cell suspension injection. All mice were euthanized at the predetermined experimental endpoint for tissue sampling. Death was confirmed by cessation of chest movement and spontaneous breathing, and the absence of a palpable heartbeat for ≥2 min.

Cell culture. The murine glioma GL261 cell line was obtained from Zhili Zhongte Biological Technology Co., Ltd. Cells were cultured in DMEM, supplemented with 10% fetal bovine serum (both Beijing Solarbio Technology Co., Ltd.,), and 100 μg/ml streptomycin. All cells were maintained at 37˚C in a humidified incubator with an atmosphere of 5% CO_2.

MRI and ^{1}H-MRS. GL261 cells were injected into the right caudate nucleus of the mice to establish the *in situ* brain tumor model. A total of 12 mice underwent regular *in vivo* scans using MRI: T2WI was performed on days 7, 14 and 21 after implantation to non-invasively evaluate the growth of the tumor tissue. Additionally, ^{1}H-MRS was used to measure brain metabolites in mice 21 days after tumor implantation. Mice were anesthetized with 3% isoflurane at 2 l/min for up to 5 min, followed by 1-1.5% isoflurane at 1 l/min consistently during the MRI scan. All MRI and MRS experiments were acquired on the horizontal 30 cm-bore preclinical 9.4T MR system (uMR 9.4T, Shanghai United Imaging Healthcare Co., Ltd.) using a volume coil with 86 mm inner diameter for radio frequency transmission and a three-channel phased array mouse brain surface coil for signal reception. To stabilize the body temperature of the mice, an animal warming system was used, which consisted of a warm water (39˚C) reservoir with a pump and hoses underneath the animal bed. The mice breathed freely during the whole MR acquisition and were monitored for changes in respiratory rate to adjust the anesthetic concentration. Body temperature and respiratory rate were kept at 36-37˚C and 60-80 bpm, respectively, using small animal vital signs monitor system (SA instruments, Inc.) during the MRI scan.

A fat suppressed T2-weighted fast spin echo sequence was performed for transverse imaging of the mouse brain to evaluate brain tumor, with the following parameters: Repetition time, 3,000 msec; echo time, 49 msec; volume of interest (VOI), 20x20 mm^2; resolution, 0.1x0.1 mm; echo spacing, 7.04 msec; echo train length, 13; slice thickness, 0.5 mm with

no gap. Imaris software (version 10.2; Oxford Instruments) was used for 3D reconstruction as well as rendering of mouse brain tumors.

Water-suppressed and non-water-suppressed MRS data of mouse brain tumor and the contralateral brain tissue were acquired using the Point Resolved Spectroscopy sequence with following parameters: Repetition time, 2,500 msec; echo time, 6 msec; VOI, 2x2x2 mm^3; bandwidth, 4,000 Hz; number of excitations (NEX), 128. After positioning of the VOI, manual shimming (defined as the manual optimization of magnetic field homogeneity within each VOI) was adjusted for each VOI. To avoid residual water signals in the spectral data caused by suboptimal shimming results, Java Based Magnetic Resonance User Interface software (version 5.2) (26) was used to suppress the water signal in the MRS data (27,28). Metabolite quantification was performed using the LCModel (version 6.3-1L) (29,30), which calculates the best fit to the experimental spectrum as a linear combination of model spectra (simulated spectra of brain metabolites). Raw data were used for the standard data input. The water-suppressed time domain data were analyzed between 0.2 and 4.0 ppm. The following metabolites were included in the basis set of simulated metabolite spectra used to model and quantify the *in vivo* MRS data: creatine (Cr), glycerophosphorylcholine (GPC), phosphorylcholine (PCh), glutathione, myo-inositol (mI), lactate (Lac), phosphocreatine (PCr), N-acetylaspartate (NAA), N-acetylaspartylglutamate (NAAG) and lipids at 1.3 ppm (Lip1.3). The absolute quantitative concentrations of metabolites in the mouse brain were calculated using the LCModel software, with reference to the internal tissue water signal. Key metabolite ratios were calculated, including tNAA/tCr, tCho/tCr, tNAA/tCho, Lip1.3/tCr, Lac/tCr and mI/tCr, where tNAA=NAA + NAAG, tCr=Cr + PCr and tCho=GPC + PCh. Additionally, the composite lipid peak at 1.3 ppm was analyzed, defined as Lip1.3=Lip1.3a (at ~1.28 ppm) + Lip1.3b (at ~1.30 ppm). The ^{1}H-MRS dataset analyzed during the present study is available in the Zenodo repository (zenodo.org/records/17759344) at the following DOI: 10.5281/zenodo.17759344.

PET-CT imaging and pharmacokinetics. Following induction with 3% isoflurane (2 l/min for up to 5 min), mice were maintained under anesthesia with 1.0-1.5% isoflurane at 1 l/min during a 2 h, whole-body FDG dynamic PET/CT scan (MadicLab PSA071, Shandong Madic Technology Co., Ltd.). At the start of the scan, mice were injected via a tail vein indwelling needle with 100 μl FDG solution, containing 8.4±0.7 MBq radioactivity. PET/CT images were reconstructed in three-dimensional reconstruction algorithm for maximum likelihood analysis (3D RAMLA; MadicLab PSA071, Shandong Madic Technology Co., Ltd.) with CT scan (80 kV, 70 mAs) for attenuation correction and fusion localization, with 0.8x0.8x0.8 mm as the final resolution. PMOD software (version 4.4, PMOD Technology GmbH) was used for data processing and image analysis. For visual assessment of tracer distribution, maximum intensity projection images were generated. Based on PET/CT imaging, VOI of the liver, kidney and bladder was manually plotted. The VOI of the tumor and the corresponding anatomically matched region on the contralateral hemisphere (serving as the background) were outlined as a sphere with a diameter of 1.5 mm. The standardized uptake value of FDG in the VOI (SUVmax) was calculated. The tumor/background (T/B) ratio was calculated as SUVmax-T/SUVmax-B. Time-activity curves (TACs) were extracted from organ VOIs.

A 2-tissue compartment model (plasma and precursor and metabolic product pool in brain tissue) was constructed (Fig. 2). k1 (ml/min/cm^3) and k2 (min^{-1}) represent the blood-to-tissue and tissue-to-blood FDG delivery rate, respectively; k3 (min^{-1}) is the FDG phosphorylation rate. This irreversible model assumes negligible FDG dephosphorylation [FDG dephosphorylation rate (k4; min^{-1}) is 0] (31). In addition, VOI placement and TAC extraction were performed for the inferior vena cava to obtain the image-derived input function. K_i was calculated to represent the net FDG influx rate, which is used to describe glucose (32).

Western blot analysis. The mice were euthanized by an overdose of 5% isoflurane delivered at 2 l/min for 5 min and perfused transcardially with cold physiological saline. The brain was dissected and tissue was immediately collected on ice and stored at -80˚C. Total protein was extracted using RIPA lysis buffer (Beyotime Institute of Biotechnology; cat. no. P0013B) supplemented with PMSF. BCA protein assay kit was used to quantify the protein concentration. The protein sample (20 μg/lane) was separated by 10% SDS-PAGE and transferred to a PVDF membrane. The membranes were blocked with 5% BSA (Wuhan Servicebio Technology; cat. no. G2052) for 1 h at room temperature. Subsequently, they were incubated overnight at 4˚C with the following primary antibodies: Glucose transporter type 1 (GLUT1, (Proteintech Group, Inc.; cat. no. 66290-1-Ig, 1:1,500) and GAPDH (Wuhan Servicebio Technology Co., Ltd.; cat. no. GB12002, 1:2,500). The next day, membranes were washed three times (10 min each) with TBST (0.1% Tween-20) and incubated with HRP-conjugated secondary antibodies (Wuhan Servicebio Technology; cat. no. GB23301, 1:5,000) at room temperature for 1 h. The membranes were washed again three times with TBST (10 min each). Protein bands were visualized using ECL reagent (Biosharp Biotechnology) and imaged with a gel imaging system. The relative gray values of the protein bands were analyzed using ImageJ (version 1.50b) software.

Morphology and pathology. The mice were euthanized by an overdose of 5% isoflurane delivered at 2 l/min for 5 min, perfused transcardially with cold physiological saline. The dissected brain was fixed in 4% PFA at 4˚C for 24 h. Following fixation, tissue underwent graded dehydration, cleared in xylene, embedded in paraffin, and sectioned at a thickness of 5 μm. For hematoxylin and eosin (HE) staining, sections were deparaffinized, rehydrated stained with hematoxylin (5-8 min) and eosin (1-3 min) at room temperature, dehydrated, cleared, and mounted. Stained sections were examined and imaged under a light microscope for morphological analysis.

Statistical analysis. All data are presented as the mean ± SD of ≥3 independent biological replicates unless otherwise specified. Statistical analysis was performed using Prism 9 (GraphPad Software, Inc.; Dotmatics). For comparisons between two groups, a paired Student's t-test was used. For comparisons among >2 groups, one-way ANOVA was performed, followed

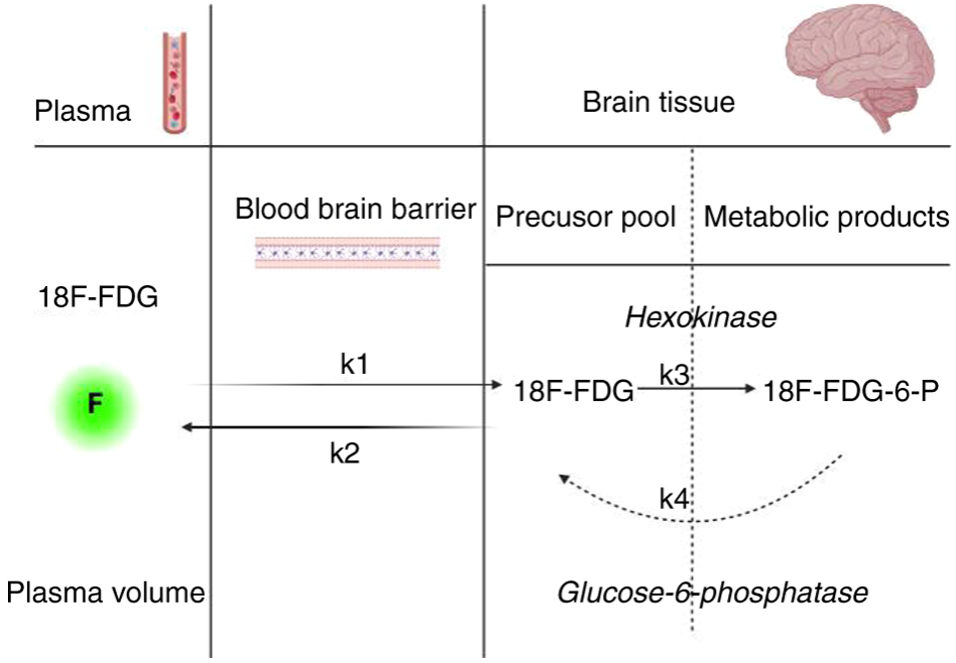

Figure 2. Model of FDG metabolism in glioblastoma mice. Two-compartments (plasma and brain tissue) and the corresponding forward transfer coefficients (k1, k2, k3, and k4) are used in the metabolism model of FDG. It is assumed that the phosphorylation of FDG (k3) is a one-way process without dephosphorylation (k4) and the forward transfer coefficient from the precursor pool in brain tissue back into the plasma is negligible as phosphorylated glucose and FDG are unable to cross the blood-brain barrier. Figure adapted from (31). k1, the transport rate of FDG from plasma into tissue; k2, the transport rate of free FDG from tissue back to plasma; FDG-6-P, fluorodeoxyglucose-6-phosphate.

by Tukey's post hoc test for multiple comparisons. $P<0.05$ was considered to indicate a statistically significant difference.

Results

Dynamic and non-invasive evaluation of GBM growth by MRI. A small animal 9.4T MRI was used to evaluate whether the GBM tumor model in the mouse brain was successfully established. The tumor was observed longitudinally 7, 14 and 21 days after injection of GL261 cells in the brain under T2WI condition. Compared with normal C57BL/6 mouse MRI (Fig. 3A), the tumor was located in the right cerebral hemisphere, with a spherical shape, relatively clear boundary between the tumor tissue and the surrounding normal brain tissue, non-uniform signal within the tumor and a small number of edema bands around the tumor (Fig. 3B-D). The midline of the brain was shifted to the left, the tumor occupying effect was notable and the right lateral ventricle had different degrees of compression and deformation (Data S1-4). The tumor grew in a time-dependent manner, measuring 1.26±0.65, 4.92±0.55 and 13.85±2.83 mm^3 on day 7, 14 and 21 respectively (Fig. 3E; Table SI).

Measurement of metabolism in GBM with ^{1}H-MRS. The metabolism in the tumor was different from that of the contralateral normal brain tissue as well as normal C57 mouse brain tissue. The levels of tCho (Fig. 4A) and the tCho/tCr ratio (Fig. 4E) were significantly increased in the tumor compared with that in the contralateral normal brain and the normal mouse brain tissue. Levels of tNAA (Fig. 4C) and tCr (Fig. 4B), key brain metabolites, were decreased in tumor compared with normal brain tissue. A notable decline in tNAA/tCho (Fig. 4F) ratio and increase in tNAA/tCr (Fig. 4D) ratio were demonstrated in the tumor compared with the contralateral and the normal mouse brain tissue. Lip1.3/tCr (Fig. 4G), Lac/tCr (Fig. 4H) and mI/tCr (Fig. 4I) in the tumor were significantly higher than in the contralateral normal brain tissue and the normal mouse brain tissue.

Detection of GBM with PET-CT. The diagnosis of tumors was confirmed using small animal PET-CT 21 days following intracerebral injection of GL261 cells in mice. FDG was rapidly distributed throughout the body of the mice after injection via the tail vein, but in the brain on the tumor side, FDG was absent for the first 6 min, after which the FDG content in the tumor tissue increased (Fig. 5F). By contrast, the FDG content in normal brain tissue decreased in a time-dependent manner (Fig. 5E). Calculation of T/B revealed a time-dependent increase (Fig. 5C), which was significantly higher at 2 h (T/B=2.23) compared with the conventional time point imaging modality of 1 h after FDG injection (T/B=1.55; Fig. 5D). SUV decreased in the kidney and liver (Fig. 5G-J), whereas SUV increased in the bladder in a time-dependent manner (Fig. 5H and L). FDG was specifically and selectively distributed in tumor tissue rather than in normal brain tissue and it was easier to differentiate tumor from normal brain tissue after extending the scan time to 2 h (Fig. 5A and B; Data S5 and S6).

Pharmacokinetics of FDG in mice with brain tumors. Pharmacokinetic analysis showed that the distribution of FDG in brain and tumor tissue was consistent with a two-compartment model. The metabolism of FDG was abnormal in the tumor compared with brain tissue in GBM mice, represented

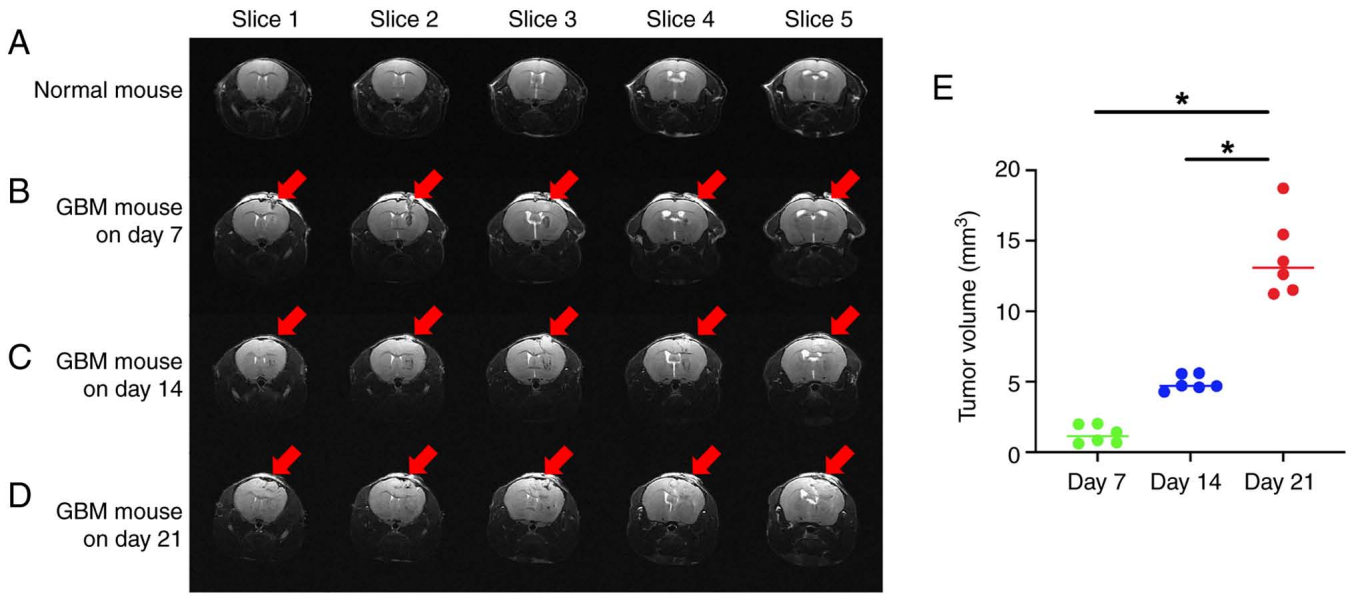

Figure 3. Dynamic and non-invasive evaluation of GBM growth by MRI. Representative T2-weighted images of brain for (A) normal C57 mice and gliomas from model mice at (B) 7, (C) 14 and (D) 21 days following cell injection (arrows indicate tumor regions). (E) At day 21, mice had a significantly increased tumor volume compared with days 7 and 14. n=6; *P<0.05. GBM, glioblastoma.

by decreased uptake of FDG and slow metabolism of FDG in the tumor tissue (k1=0.797 vs. 1.844 for the uptake, k2=2.722 vs. 3.844 for the metabolism, k3=0.319 vs. 0.280 for the phosphorylation, vB=2.3% vs. 3.6% for blood volume fraction, K_i=0.084 vs. 0.125 for the FDG net influx rate); values in normal mice were as follows: k1=1.530, k2=3.218, k3=0.426, vB=2.8% and K_i=0.179 (Table I).

GLUT1 protein expression in brain tissue and tumor tissue. To investigate the specific molecular mechanisms underlying glucose uptake in glioma, the present study analyzed the protein expression levels of GLUT1 (Fig. 6A) in brain and tumor tissue. Compared with normal brain tissue, glioma tissue exhibited significantly elevated GLUT1 protein levels (Fig. 6B).

Morphological and pathological analysis. Morphological analysis confirmed the formation of tumors in the brain of GBM mice detected by MRI and PET-CT, along with pathological changes in tissue structure (Fig. 7A and B). HE staining showed notable heterogeneity of tumor cells (tumor cells varied in size, distinct nucleoli, abundant and eosinophilic cytoplasm, mitotic figures), accompanied by focal necrosis (Fig. 7C-E).

Discussion

The present study established a mouse GBM model and characterized gliomas in GL261 mice by 9.4T high field small animal MRI and PET-CT. The present study established a methodological framework for investigation of tumor characteristics and molecular mechanisms of GBM.

GBM is the most common type of primary malignant brain tumor in adults (1,8,32). Surgical tumor resection followed by concurrent chemoradiotherapy along with adjuvant temozolomide is the current standard therapy for patients with GBM (33). Accurate diagnosis and clinical staging of gliomas are key for clinical decision-making and treatment planning. Advances in imaging technology, particularly the application of MRI and PET-CT, have provided powerful tools for diagnosing glioma (34). These imaging modalities enable direct visualization, dynamic assessment, non-invasive procedures and quantitative analysis, thereby facilitating early diagnosis and more effective treatment, ultimately contributing to reduced mortality rates (35,36). While the gold standard for confirming the grading of glioma remains pathological testing, numerous findings (37-41) have shown that MRS helps imaging physicians more accurately and non-invasively assess the histological grade, molecular profile, prognosis and effectiveness of novel therapies in patients with glioma. The primary metabolites of glioma used in clinical practice include tNAA, tCr, tCho, Lac and their ratio (42). However, the spectral resolution of ^{1}H-MRS is dependent on the magnetic field strength. A higher field strength increases the frequency separation between metabolite peaks at a given chemical shift, thereby improving spectral resolution and allowing detection of more metabolite information (43,44). Therefore, the mouse model with 9.4T high field was used to observe characteristics of tumor metabolites in an *in situ* glioma model.

The present study compared the metabolism between brain tumors, normal brain tissue of tumor-bearing mice and normal mouse brain tissues using ^{1}H-MRS. Of particular relevance to tumor biology is the metabolism of choline-containing compounds, which reflects cell membrane turnover and proliferation (45). Specifically, the levels of tCho and the ratio of tCho/tCr were significantly increased in the tumor. These alterations are associated with the degree of malignancy and mitotic activity of GBM (45,46), and the elevated tCho/tCr ratio indicated that the tumor cells were proliferating actively. It has been hypothesized that the tCho/tCr ratio may predict the expression of microchromosome maintenance protein 2 to non-invasively assess cell proliferation activity as a marker of energy metabolism (47,48). In addition, levels of tNAA, a

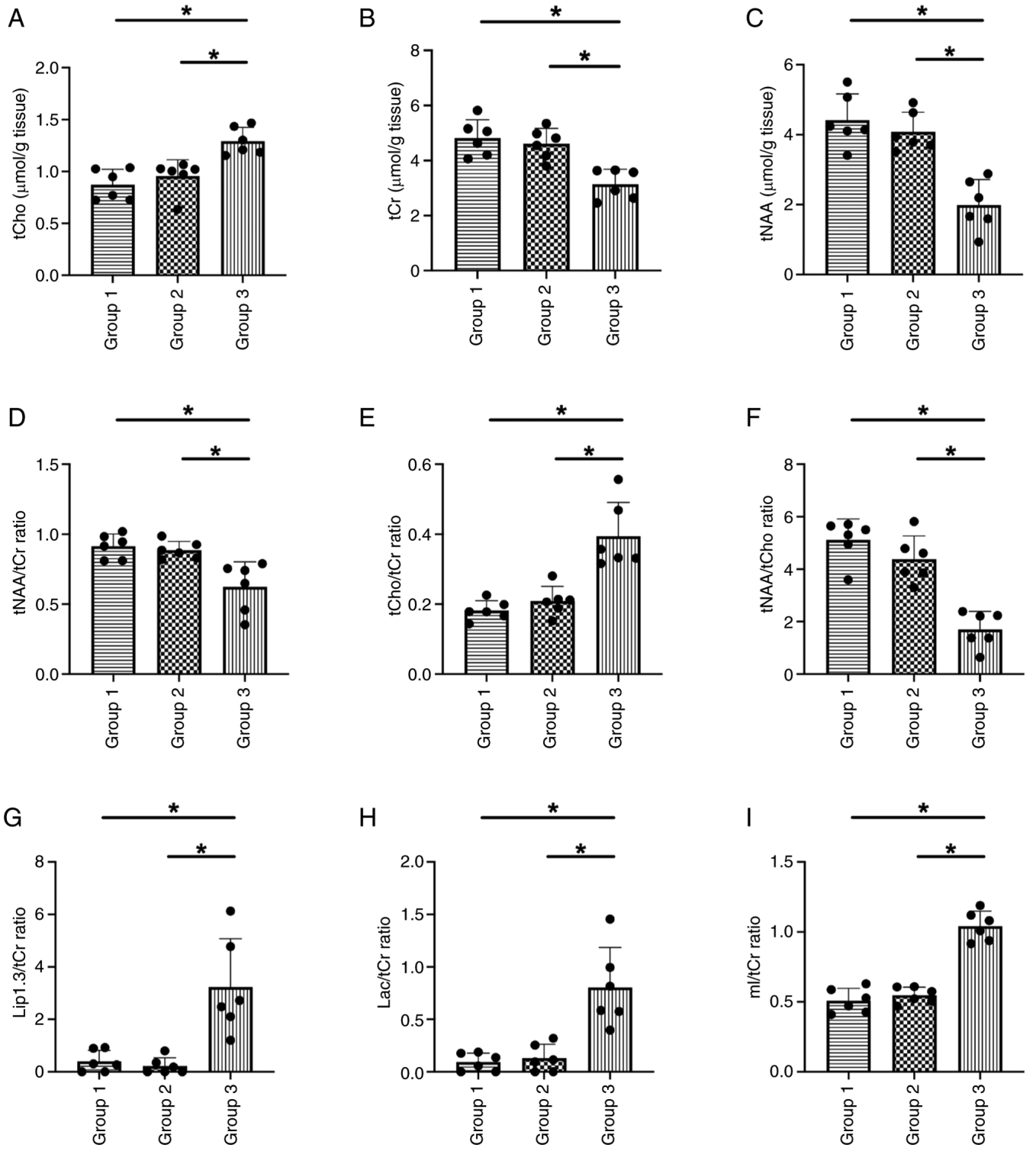

Figure 4. Mean metabolite concentration and ratios with tCr in normal and GBM mice. The peak area measurements of the metabolites were used to calculate the metabolite concentrations and ratios relative to (A): tCho, (B) tCr and (C) tNAA concentration and (D) tNAA/tCr, (E) tCho/tCr, (F) tNAA/tCho (F); Lip1.3/tCr ratio (G); Lac/tCr ratio (H); mI/tCr ratio (I). n=6. *P<0.05. Group 1, normal mouse; group 2, normal contralateral brain tissue of GBM mouse; group 3, tumor tissue of GBM mouse. tCr, total creatine; GBM, glioblastoma; tCho, total choline; tNAA, total N-acetylaspartate; Lip1.3, lipids at 1.3 ppm; Lac, lactate; mI, myo-inositol.

key brain metabolite as a marker of neuronal integrity, were significantly decreased in tumor tissue. NAA is one of the most concentrated neurometabolites in the brain. In neuronal mitochondria, NAA is synthesized from the substrates acetyl CoA and aspartate (47). The tNAA/tCr and the tNAA/tCho ratio demonstrated a notable decrease in tumor tissue. These changes indicate neuronal loss or dysfunction due to tumor invasion and displacement. In a retrospective study evaluating the association between MRS and the grading of glioma, it was found that NAA/Cho and NAA/Cr were negatively associated and Cho/Cr was positively associated with pathological grading in patients with glioma (9). These findings are useful for

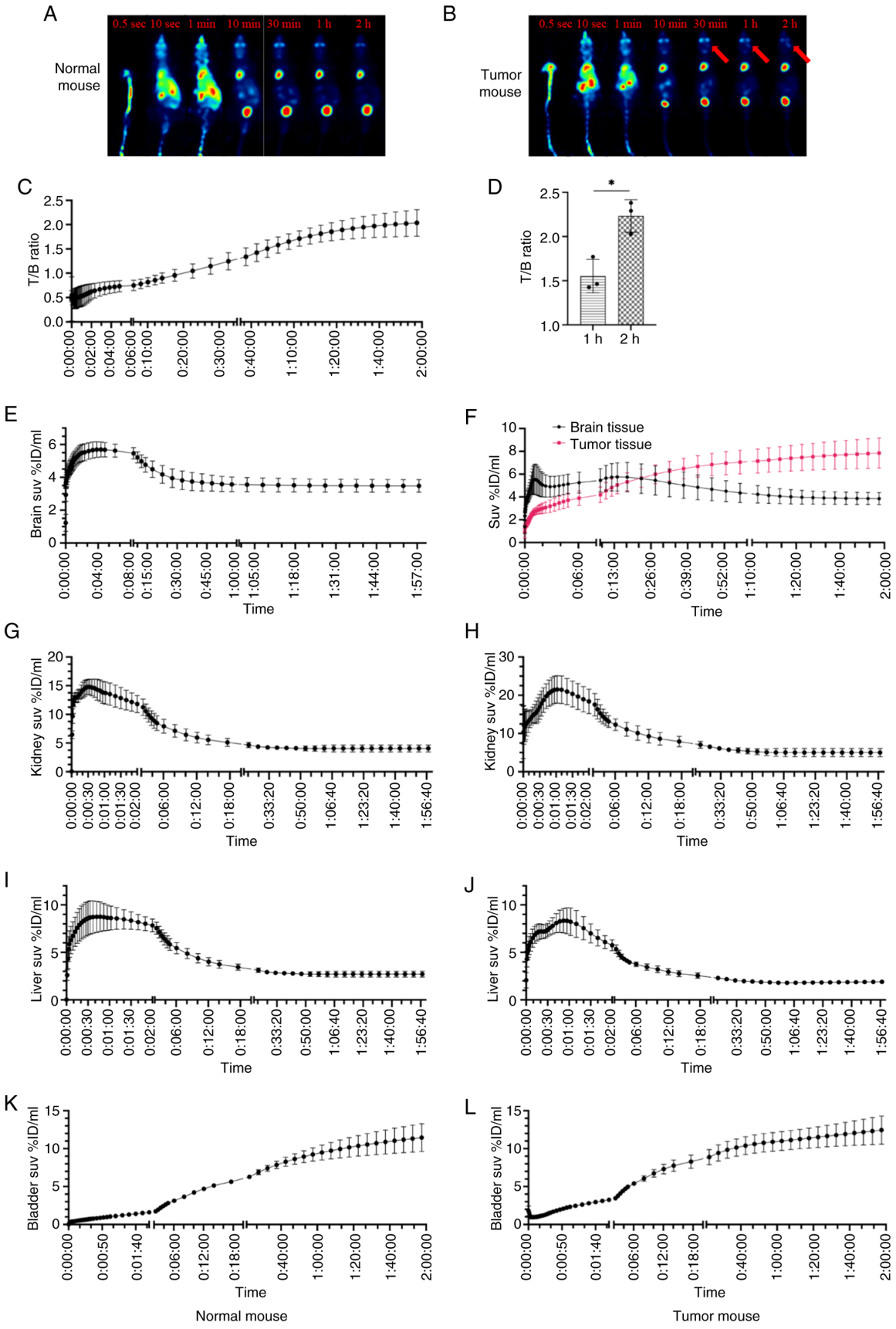

Figure 5 Characteristics of FDG imaging in tumor and normal mouse. (A) Normal and (B) tumor mice. Arrow, tumor regions. FDG was specifically and selectively distributed in tumor tissue rather than in normal brain tissue after extending the scan time to 2 h. There was a time-dependent increase in the T/B ratio (C). Comparison of T/B ratios at 1 and 2 h after FDG injection revealed that the 2 h T/B ratio was significantly higher than the 1 h T/B ratio (D). FDG was rapidly distributed throughout the body of the mice (E), but in the brain on the tumor side, FDG was absent for the first 6 min, after which the FDG content in the tumor tissue increased (F). SUV values in the normal mice kidneys (G), tumor mice kidneys (H), normal mice livers (I) and tumor mice livers (J) gradually decreased over time. Conversely, SUV values in the normal mice bladders (K) and tumor mice bladders (L) exhibited a time dependent upward trend. n=3. *P<0.05. T/B, tumor tissue/background; FDG, ^{18}F-fluorodeoxyglucose; SUV, standardized uptake value; ID, injected dose.

Table I. Pharmacokinetics of FDG in normal and tumor mice.

	Normal mouse				Tumor mouse				
Parameter	Brain	Liver	Kidney	Bladder	Brain	Tumor	Liver	Kidney	Bladder
vB	0.028	0.036	0.051	0.012	0.036	0.023	0.057	0.267	0.024
k1	1.530	2.922	7.497	0.181	1.844	0.797	3.677	7.975	0.211
k2	3.218	2.583	3.325	0.023	3.844	2.722	4.462	4.120	0.076
k3	0.426	0.000	2.297	0.081	0.280	0.319	0.014	3.264	0.037
Vt	1.553	0.081	1.558	10.964	2.250	4.941	0.954	3.613	13.850
Vs	0.985	1.262	3.324	2.762	1.758	4.499	0.084	1.790	2.725
k1/k2	0.568	1.141	2.481	8.203	0.490	0.442	0.870	2.025	4.432
Flux	0.182	0.000	3.144	0.092	0.133	0.083	0.015	3.722	0.049
AUC	27028.321	21747.060	50661.858	88515.180	31927.733	47218.743	15373.799	44143.267	72962.892
Ki	0.179	0.000	3.063	0.141	0.125	0.084	0.011	3.525	0.069

Pharmacokinetic analysis showed that the distribution of FDG in brain and tumor tissues was consistent with a two-compartment model. Compared with brain tissue, tumor tissue had less FDG uptake and slow FDG metabolism. n=3. vB, blood volume fraction; k1, uptake rate constant; k2, clearance rate constants; k3, phosphorylation rate constant; Vt, total volume of distribution; Vs, specific binding concentration; k1/k2, volume of distribution of organ; AUC, area under the curve; Ki, net FDG inflow rate; FDG, ^{18}F-fluoro-deoxyglucose.

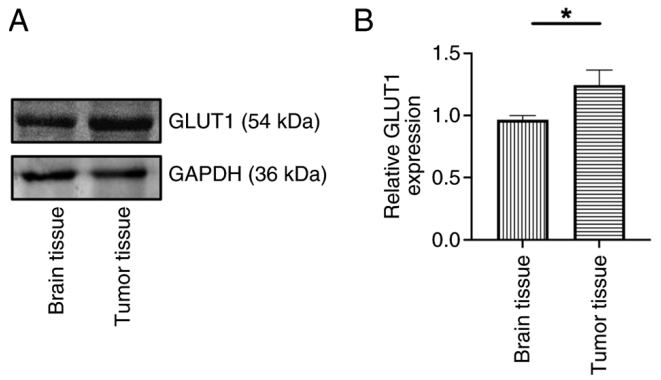

Figure 6. Protein expression of GLUT1. (A) Western blotting was performed to determine (B) expression of GLUT1 protein. n=3. *P<0.05. GLUT1, glucose transporter type1.

preoperative diagnostic prediction of glioma. The present study also found an increase in the Lac and lipid peaks in the tumor tissue. When the proliferation rate of GBM increases rapidly, it may lead to increased Lac/tCr and lipid (Lip1.3/tCr) levels due to local hypoxia and tissue necrosis (48). Clinically, clear lipid peaks may be associated with grade IV tumors (49,50). Therefore, the GL261 glioma model may have certain characteristics of a grade IV glioma, which is more malignant. mI is a basic sugar produced primarily by astrocytes and is a component of key molecules such as inositol phosphates and phosphatidylinositol (44). Here, the mI/tCr ratio was increased in brain tumors compared with normal brain tissue. In glioma, increased mI concentration has also been evaluated as a marker of astrocytopathy, typically accompanied by changes in Cr and other metabolites (49,51,52).

Following dynamic 2 h PET-CT scanning of the whole body of the mice, it was possible to detect whether distant metastasis of GBM had occurred. In addition, the metabolism of FDG in other organs (liver, kidney and bladder) was analyzed, demonstrating a decrease in SUV values in the heart, liver and kidney, and an increase in the SUV values of the bladder over time, which is consistent with the metabolic profile of FDG. Attempts have been made to differentiate normal cortical hypermetabolism from high-grade lesions by delayed acquisition imaging, but this has been inconclusive due to patient compliance issues (53). The present study assessed whether delayed dynamic FDG imaging of untreated GBM offers a diagnostic advantage compared with the conventional imaging time point of ~1 h following tracer injection. FDG was not distributed for the first 6 min, then the tumor region showed a gradual increase in SUV value, with a gradual decrease in SUV in normal brain tissue. It was hypothesized that the increasing T/B contrast over time results from differential tracer clearance rates. Normal brain tissue rapidly clears unbound FDG, while tumor cells, due to upregulated GLUT1 and hexokinase activity, trap FDG-6-phosphate intracellularly, leading to progressive signal accumulation. This phenomenon may be attributed to the upregulation of GLUT1 in tumor cells (54). Under physiological conditions, GLUT1 is predominantly localized at the blood-brain barrier, where it facilitates basal glucose transport (55). In high-grade glioma, however, neoplastic cells demonstrate upregulated GLUT1 expression and enhanced hexokinase activity. Following cellular uptake, FDG is phosphorylated by hexokinase to FDG-6-phosphate, which cannot be further metabolized via glycolysis. This leads to its effective entrapment within tumor cells, resulting in radiotracer accumulation and clear visualization of malignant lesions on imaging (56). The present western blot results, which confirmed elevated GLUT1 expression in tumor tissue, provided direct molecular support for this mechanism. In clinical practice, regions with high FDG uptake correspond to the tumor core, characterized by intense metabolic activity, and are associated with a higher pathological grade. This association offers a rational basis for improving the discrimination

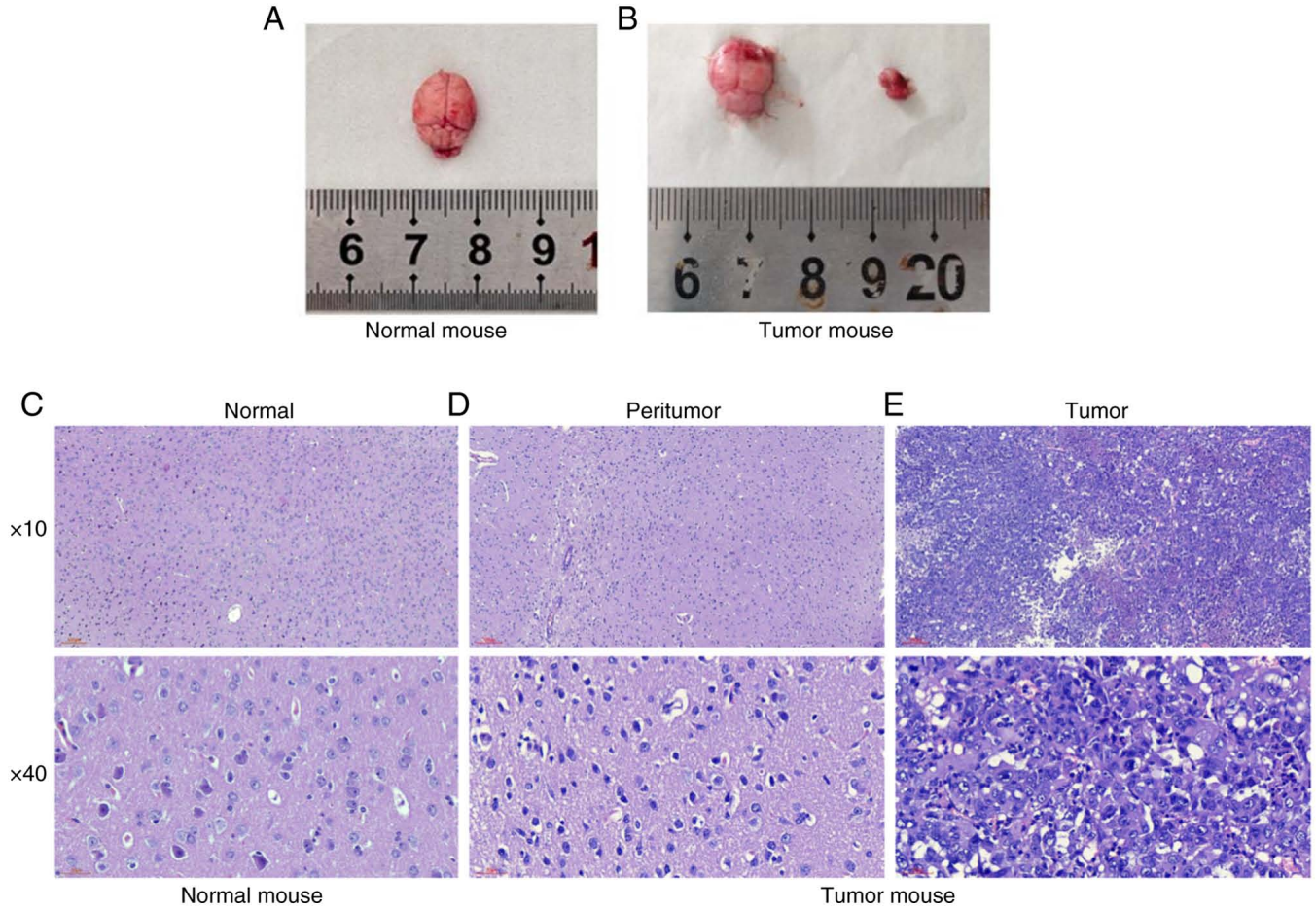

Figure 7. Gross and microscopic pathology of glioma and brain tissue. Brain tissue of (A) normal mice was structurally intact, while that of (B) tumor-bearing mice was incomplete, and the tumor tissue was accompanied by necrotic hemorrhage. Hematoxylin-eosin staining of (C) brain, (D) peritumor and (E) tumor tissue showed heterogeneity of tumor cells (tumor cells varied in size, distinct nucleoli, abundant and eosinophilic cytoplasm, mitotic figures), accompanied by focal necrosis.

between tumor recurrence and treatment-associated changes, thereby facilitating more precise clinical decision-making (57).

Gross dissection of GBM mouse brain revealed necrosis within the tumor tissue. The pathological findings revealed by HE staining validated the detection results of ^{1}H-MRS and PET-CT, confirming necrotic areas and an invasive growth pattern which were consistent with the pathological characteristics.

The present study used a multimodal, multi-level research strategy, which integrated *in vivo* non-invasive imaging with *ex vivo* molecular and morphological analysis. This approach enables a comprehensive assessment of mouse brain glioma. However, the present study has certain limitations. Firstly, all experiments were conducted using mouse models, which exhibit notable species differences from human patients in tumor microenvironment composition, immune response characteristics and disease progression dynamics. Consequently, it is challenging to simulate the complex pathological features and heterogeneity of human brain glioma, limiting clinical translation. Secondly, the present study primarily focused on observing and describing the disease state without incorporating any therapeutic intervention. Consequently, the sensitivity and clinical utility of the multimodal assessment system for monitoring treatment efficacy remain unverified. Thirdly, use of only three model and three control mice may limit the statistical power of some analyses and increase the influence of individual variability. However, the present findings are in agreement with previously published reports (37,49,58), which strengthens the reliability of the conclusions.

In summary, the present study established a mouse glioblastoma model. High-field MRI was used for non-invasive assessment of brain gliomas in mice, while MRS was used to analyze the metabolic processes of brain tumors. Combined with non-invasive metabolic imaging via PET-CT and molecular-level analysis of GLUT1 protein expression, the present approach provided robust and consistent evidence for the key role of high glycolysis in this mouse glioblastoma model. Finally, pathological evaluation was supplemented by HE staining.

Acknowledgements

Not applicable.

Funding

The present study was supported by Fundamental Research Funds for the Central Universities of Lanzhou

University (grant no. lzujbky-2022-sp08); Medical Research Improvement Project of Lanzhou University (grant no. lzuyxcx-2022-154); Medical Innovation and Development Project of Lanzhou University (grant no. lzuyxcx-2022-141); Major Science and Technology Project of Gansu Province (grant nos. 22ZD6FA050, 22JR9KA002, 23YFFA0047 and 20ZD7FA003); Project of Gansu Provincial Department of Education (grant no. 2021jyjbgs-02); Project of Gansu Provincial Development and Reform Commission (grant no. 2020-20240); Natural Science Foundation of Gansu Province (grant nos. 21JR1RA135 and 23JRRA1001); National Natural Science Foundation of China (grant nos. 81960673, 81870329 and 82260612) and 2023 Lanzhou Science and Technology Plan Project and Talent Innovation and Entrepreneurship Project (grant no. ZX-62000001-2023-015).

Availability of data and materials

The data generated in the present study may be requested from the corresponding author.

Authors' contributions

FT, XZ and YL conceived and designed the study. SL, WG and YJ interpreted MRI and PET-CT data. TL, LS and YujW established the mouse model. SL and WG wrote the manuscript. YS, HJ, ZW, YucW and BW analyzed data. YL and FT supervised the study and confirm the authenticity of all the raw data. All authors have read and approved the final manuscript.

Ethics approval and consent to participate

All experimental procedures were conducted according to the guidelines for the care and handling of laboratory animals recommended by the National Institutes of Health and the protocol was approved by the Ethics Committee of Lanzhou University Second Hospital (approval no. D2025-787), Lanzhou, China.

Patient consent for publication

Not applicable.

Competing interests

The authors declare that they have no competing interests.

References

1. Bathla G, Dhruba DD, Liu Y, Le NH, Soni N, Zhang H, Mohan S, Roberts-Wolfe D, Rathore S, Sonka M, *et al*: Differentiation between glioblastoma and metastatic disease on conventional MRI imaging using 3D-convolutional neural networks: Model development and validation. Acad Radiol 31: 2041-2049, 2024.
2. Bonada M, Rossi LF, Carone G, Panico F, Cofano F, Fiaschi P, Garbossa D, Di Meco F and Bianconi A: Deep learning for MRI segmentation and molecular subtyping in glioblastoma: Critical aspects from an emerging field. Biomedicines 12: 1878, 2024.
3. Wang J, Liu G and Wang J: Prediction of O6-methylguanine-DNA ethyhransferase methylation status in glioblastoma based on deep learning. J Lanzhou Univ (Med Sci) 49: 50-55, 2023.
4. Schaff LR and Mellinghoff IK: Glioblastoma and other primary brain malignancies in adults: A review. JAMA 329: 574-587, 2023.
5. Price M, Ballard C, Benedetti J, Neff C, Cioffi G, Waite KA, Kruchko C, Barnholtz-Sloan JS and Ostrom QT: CBTRUS statistical report: Primary brain and other central nervous system tumors diagnosed in the United States in 2017-2021. Neuro Oncol 26 (Suppl_6): vi1-vi85, 2024.
6. Chan P, Rich JN and Kay SA: Watching the clock in glioblastoma. Neuro Oncol 25: 1932-1946, 2023.
7. Deng J, Li S and Huang X: Quantitative evaluation of the therapeutic effect of temozolomide on rat C6 glioma by spectral CT imaging. J Lanzhou Univ (Med Sci) 49: 25-31, 2023.
8. Chelliah A, Wood DA, Canas LS, Shuaib H, Currie S, Fatania K, Frood R, Rowland-Hill C, Thust S, Wastling SJ, *et al*: Glioblastoma and radiotherapy: A multicenter AI study for Survival Predictions from MRI (GRASP study). Neuro Oncol 26: 1138-1151, 2024.
9. Hesse F, Low J, Cao J, Bulat F, Kreis F, Wright AJ and Brindle KM: Deuterium MRI of serine metabolism in mouse models of glioblastoma. Magn Reson Med 92: 1811-1821, 2024.
10. In't Zandt R, Mahmutovic Persson I, Tibiletti M, von Wachenfeldt K, Parker GJM and Olsson LE; TRISTAN Consortium: Contrast enhanced longitudinal changes observed in an experimental bleomycin-induced lung fibrosis rat model by radial DCE-MRI at 9.4T. PLoS One 19: e0310643, 2024.
11. Kodama N, Setoi A and Kose K: Spiral MRI on a 9.4T vertical-bore superconducting magnet using unshielded and self-shielded gradient coils. Magn Reson Med Sci 17: 174-183, 2018.
12. Tripathi M, D'Souza M, Bal J, Guliani S, Jain J, Santosh, Sharma R and Mondal A: Comparision of F-18 FDG and C-11 methionine PET/CT for demonstration of subependymal deposit in a treated case of glioblastoma multiforme. Indian J Nucl Med 26: 91-93, 2011.
13. Zhou W, Wen J, Hua F, Xu W, Lu X, Yin B, Geng D and Guan Y: ^{18}F-FDG PET/CT in immunocompetent patients with primary central nervous system lymphoma: Differentiation from glioblastoma and correlation with DWI. Eur J Radiol 104: 26-32, 2018.
14. Malik D: FDG PET/CT in recurrent glioblastoma multiforme with leptomeningeal and diffuse spinal cord metastasis. Clin Nucl Med 46: 138-139, 2021.
15. Kim SH, Lee SJ and Yu SM: Study of lipid proton difference evaluation via 9.4T MRI analysis of fatty liver induced by exposure to methionine and choline-deficient (MCD) diet and high-fat diet (HFD) in an animal model. Chem Phys Lipids 242: 105164, 2022.
16. Pudelko L, Edwards S, Balan M, Nyqvist D, Al-Saadi J, Dittmer J, Almlöf I, Helleday T and Bräutigam L: An orthotopic glioblastoma animal model suitable for high-throughput screenings. Neuro Oncol 20: 1475-1484, 2018.
17. Hsu W, Siu IM, Pradilla G, Gokaslan ZL, Jallo GI and Gallia GL: Animal model of intramedullary spinal cord glioma using human glioblastoma multiforme neurospheres. J Neurosurg Spine 16: 315-319, 2012.
18. Underhill HR: A continuous-infusion dynamic MRI model at 3.0 Tesla for the serial quantitative evaluation of microvascular proliferation in an animal model of glioblastoma multiforme. Magn Reson Med 78: 1824-1838, 2017.
19. Bolcaen J, Descamps B, Deblaere K, Boterberg T, Hallaert G, Van den Broecke C, Decrock E, Vral A, Leybaert L, Vanhove C and Goethals I: MRI-guided 3D conformal arc micro-irradiation of a F98 glioblastoma rat model using the Small Animal Radiation Research Platform (SARRP). J Neurooncol 120: 257-266, 2014.
20. Helthuis JHG, van der Zwan A, van Doormaal TPC, Bleys RLAW, Harteveld AA, van der Toorn A, Brozici M, Hendrikse J and Zwanenburg JJM: High resolution 7T and 9.4T-MRI of human cerebral arterial casts enables accurate estimations of the cerebrovascular morphometry. Sci Rep 8: 14235, 2018.
21. Tang H, Zhang Y, Dai C, Ru T, Li J, Chen J, Zhang B, Zhou K, Lv P, Liu R, *et al*: Postmortem 9.4-T MRI for fetuses with congenital heart defects diagnosed in the first trimester. Front Cardiovasc Med 8: 764587, 2021.
22. Yun TJ, Cho HR, Choi SH, Kim H, Won JK, Park SW, Kim JH, Sohn CH and Han MH: Antiangiogenic Effect of bevacizumab: Application of arterial spin-labeling perfusion MR imaging in a rat glioblastoma model. AJNR Am J Neuroradiol 37: 1650-1656, 2016.
23. Nickel A, Milford D, Fischer M, Bendszus M and Heiland S: Effect of contrast agent dosage on longitudinal relaxation time, signal and apparent tumor volume in glioblastoma at 9.4T. Z Med Phys 29: 206-215, 2019.

24. Louis DN, Perry A, Wesseling P, Brat DJ, Cree IA, Figarella-Branger D, Hawkins C, Ng HK, Pfister SM, Reifenberger G, *et al*: The 2021 WHO classification of tumors of the central nervous system: A summary. Neuro Oncol 23: 1231-1251, 2021.
25. Hooper GW, Ansari S, Johnson JM and Ginat DT: Advances in the radiological evaluation of and theranostics for glioblastoma. Cancers (Basel) 15: 4162, 2023.
26. Naressi A, Couturier C, Devos JM, Janssen M, Mangeat C, de Beer R and Graveron-Demilly D: Java-based graphical user interface for the MRUI quantitation package. Magma 12: 141-152, 2001.
27. Mandal PK: In vivo proton magnetic resonance spectroscopic signal processing for the absolute quantitation of brain metabolites. Eur J Radiol 81: e653-e664, 2012.
28. Jabłoński M, Starčuková J and Starčuk Z Jr: Processing tracking in jMRUI software for magnetic resonance spectra quantitation reproducibility assurance. BMC Bioinformatics 18: 56, 2017.
29. Provencher SW: Estimation of metabolite concentrations from localized in vivo proton NMR spectra. Magn Reson Med 30: 672-679, 1993.
30. Provencher SW: Automatic quantitation of localized in vivo 1H spectra with LCModel. NMR Biomed 14: 260-264, 2001.
31. Spence AM, Muzi M, Mankoff DA, O'Sullivan SF, Link JM, Lewellen TK, Lewellen B, Pham P, Minoshima S, Swanson K and Krohn KA: 18F-FDG PET of gliomas at delayed intervals: Improved distinction between tumor and normal gray matter. J Nucl Med 45: 1653-1659, 2004.
32. Jansen JF, Schöder H, Lee NY, Stambuk HE, Wang Y, Fury MG, Patel SG, Pfister DG, Shah JP, Koutcher JA and Shukla-Dave A: Tumor metabolism and perfusion in head and neck squamous cell carcinoma: Pretreatment multimodality imaging with 1H magnetic resonance spectroscopy, dynamic contrast-enhanced MRI, and [18F]FDG-PET. Int J Radiat Oncol Biol Phys 82: 299-307, 2012.
33. Zhang Y, Zhang H, Zhang H, Ouyang Y, Su R, Yang W and Huang B: Glioblastoma and solitary brain metastasis: Differentiation by integrating demographic-MRI and Deep-learning radiomics signatures. J Magn Reson Imaging 60: 909-920, 2024.
34. Tsiouris S, Bougias C and Fotopoulos A: Principles and current trends in the correlative evaluation of glioma with advanced MRI techniques and PET. Hell J Nucl Med 22: 206-219, 2019.
35. Fan H, Luo Y, Gu F, Tian B, Xiong Y, Wu G, Nie X, Yu J, Tong J and Liao X: Artificial intelligence-based MRI radiomics and radiogenomics in glioma. Cancer Imaging 24: 36, 2024.
36. Molina D, Perez-Beteta J, Luque B, Arregui E, Calvo M, Borras JM, Lopez C, Martino J, Velasquez C, Asenjo B, *et al*: Tumour heterogeneity in glioblastoma assessed by MRI texture analysis: A potential marker of survival. Br J Radiol 89: 20160242, 2016.
37. Clément A, Doyen M, Fauvelle F, Hossu G, Chen B, Barberi-Heyob M, Hirtz A, Stupar V, Lamiral Z, Pouget C, *et al*: In vivo characterization of physiological and metabolic changes related to isocitrate dehydrogenase 1 mutation expcression by multiparametric MRI and MRS in a rat model with orthotopically grafted human-derived glioblastoma cell lines. NMR Biomed 34: e4490, 2021.
38. Kumar M, Arlauckas SP, Saksena S, Verma G, Ittyerah R, Pickup S, Popov AV, Delikatny EJ and Poptani H: Magnetic resonance spectroscopy for detection of choline kinase inhibition in the treatment of brain tumors. Mol Cancer Ther 14: 899-908, 2015.
39. Shukla G, Alexander GS, Bakas S, Nikam R, Talekar K, Palmer JD and Shi W: Advanced magnetic resonance imaging in glioblastoma: A review. Chin Clin Oncol 6: 40, 2017.
40. Aleid AM, Alrasheed AS, Aldanyowi SN and Almalki SF: Advanced magnetic resonance imaging for glioblastoma: Oncology-radiology integration. Surg Neurol Int 15: 309, 2024.
41. Han X, Xiao K, Bai J, Li F, Cui B, Cheng Y, Liu H and Lu J: Multimodal MRI and ^{1}H-MRS for preoperative stratification of high-risk molecular subtype in adult-type diffuse gliomas. Diagnostics (Basel) 14: 2569, 2024.
42. Wang L, Chen G and Dai K: Hydrogen proton magnetic resonance spectroscopy (MRS) in differential diagnosis of intracranial tumors: A systematic review. Contrast Media Mol Imaging 2022: 7242192, 2022.
43. Wilson M, Andronesi O, Barker PB, Bartha R, Bizzi A, Bolan PJ, Brindle KM, Choi IY, Cudalbu C, Dydak U, *et al*: Methodological consensus on clinical proton MRS of the brain: Review and recommendations. Magn Reson Med 82: 527-550, 2019.
44. Henning A: Proton and multinuclear magnetic resonance spectroscopy in the human brain at ultra-high field strength: A review. Neuroimage 168: 181-198, 2018.
45. Tran D, Nguyen DH, Nguyen HK, Nguyen-Thanh VA, Dong-Van H and Nguyen MD: Diagnostic performance of MRI perfusion and spectroscopy for brainstem glioma grading. Eur Rev Med Pharmacol Sci 26: 7938-7948, 2022.
46. Shi Y, Liu D, Kong Z, Liu Q, Xing H, Wang Y, Wang Y and Ma W: Prognostic value of choline and other metabolites measured using ^{1}H-magnetic resonance spectroscopy in gliomas: A meta-analysis and systemic review. Metabolites 12: 1219, 2022.
47. Li J, Sun J, Wang N and Zhang Y: Study on the relationship between MRI functional imaging and multiple immunohistochemical features of glioma: A noninvasive and more precise glioma management. Mol Imaging 23: 15353508241261583, 2024.
48. Gao W, Wang X, Li F, Shi W, Li H and Zeng Q: Cho/Cr ratio at MR spectroscopy as a biomarker for cellular proliferation activity and prognosis in glioma: Correlation with the expression of minichromosome maintenance protein 2. Acta Radiol 60: 106-112, 2019.
49. Bhaduri S, Kelly CL, Lesbats C, Sharkey J, Ressel L, Mukherjee S, Platt MD, Delikatny EJ and Poptani H: Metabolic changes in glioblastomas in response to choline kinase inhibition: In vivo MRS in rodent models. NMR Biomed 36: e4855, 2023.
50. Nakamura H, Doi M, Suzuki T, Yoshida Y, Hoshikawa M, Uchida M, Tanaka Y, Takagi M and Nakajima Y: The significance of lactate and lipid peaks for predicting primary neuroepithelial tumor grade with proton MR spectroscopy. Magn Reson Med Sci 17: 238-243, 2018.
51. Hnilicová P, Richterová R, Kantorová E, Bittšanský M, Baranovičová E and Dobrota D: Proton MR spectroscopic imaging of human glioblastomas at 1.5 Tesla. Gen Physiol Biophys 36: 531-537, 2017.
52. Steidl E, Pilatus U, Hattingen E, Steinbach JP, Zanella F, Ronellenfitsch MW and Bähr O: Myoinositol as a biomarker in recurrent glioblastoma treated with bevacizumab: A 1H-magnetic resonance spectroscopy study. PLoS One 11: e0168113, 2016.
53. Zajkowska K, Cegla P and Dedecjus M: Role of [^{18}F]FDG PET/CT in the management of follicular cell-derived thyroid carcinoma. Cancer Imaging 24: 147, 2024.
54. Li T, Xu D, Ruan Z, Zhou J, Sun W, Rao B and Xu H: Metabolism/immunity dual-regulation thermogels potentiating immunotherapy of glioblastoma through lactate-excretion inhibition and PD-1/PD-L1 blockade. Adv Sci (Weinh) 11: e2310163, 2024.
55. Patching SG: Glucose transporters at the blood-brain barrier: Function, regulation and gateways for drug delivery. Mol Neurobiol 54: 1046-1077, 2017.
56. Hatano T, Zhao S, Zhao Y, Nishijima K, Kuno N, Hanzawa H, Sakamoto T, Tamaki N and Kuge Y: Biological characteristics of intratumoral [F-18]-fluoromisonidazole distribution in a rodent model of glioma. Int J Oncol 42: 823-830, 2013.
57. Stocksdale B, Nagpal S, Hixson JD, Johnson DR, Rai P, Shivaprasad A and Tremont-Lukats IW: Neuro-oncology practice clinical debate: Long-term antiepileptic drug prophylaxis in patients with glioma. Neurooncol Pract 7: 583-588, 2020.
58. Doblas S, He T, Saunders D, Hoyle J, Smith N, Pye Q, Lerner M, Jensen RL and Towner RA: In vivo characterization of several rodent glioma models by 1H MRS. NMR Biomed 25: 685-694, 2012.